Geosciences Faculty Publications and Presentations

Department of Geosciences

4-2021

A Broad, Distributed Active Fault Zone Lies Beneath Salt Lake City, Utah

Lee M. Liberty
Boise State University

James St. Clair
Pacific Northwest National Laboratory

Adam P. McKean
Utah Geological Survey

A Broad, Distributed Active Fault Zone Lies beneath Salt Lake City, Utah

Lee M. Liberty[*1] , James St. Clair[2] , and Adam P. McKean[3]

Abstract

Although the Wasatch fault is currently known to have a high-seismic hazard from motion along range-bounding faults, new seismic data reveal faulted and folded 13,000–30,000-yr-old Lake Bonneville strata beneath Salt Lake City (SLC). Coupled with previous excavation trench, borehole, and other geologic and geophysical observations, we conclude that a zone of latest Pleistocene and/or Holocene faulting and folding kinematically links the East Bench and Warm Springs faults through a 3 km wide relay structure and transfer zone. We characterize faults beneath downtown SLC as active, and these faults may displace or deform the ground surface during an earthquake. Through offset but linked faults, our observations support throughgoing ruptures across faults of the Wasatch fault zone (WFZ) and an elevated risk of earthquake-induced building damage.

Introduction

The active, 350 km long Wasatch fault zone (WFZ) defines the eastern boundary of the Basin and Range Province in northern Utah (Fig. 1). The urbanized part of the WFZ is composed of five tectonic segments with a complex earthquake record (summarized by DuRoss *et al.*, 2016). Evidence for at least 24 large-magnitude earthquakes since about 7 ka supports the possibility of a large magnitude ($M \sim 7$) surface-rupturing earthquake along the Salt Lake City (SLC) segment. The downtown SLC area lies within a left step between the East Bench fault (EBF) and Warm Springs fault (WSF) of the SLC segment (Personius and Scott, 1992; Fig. 2). A major earthquake on these faults could produce significant ground amplification of low-velocity basin sediments in the SLC metropolitan area (e.g., Roten *et al.*, 2011; Moschetti *et al.*, 2017). Although rupture of the entire SLC segment has been considered, the behavior and interaction of individual faults is unknown. Connecting two faults of the SLC segment supports a multifault rupture model and the possibility of earthquake-induced surface rupture. Here, we present new seismic reflection data that image late Quaternary lacustrine strata, and new *P*-wave (V_P) and *S*-wave (V_S) tomographic images that characterize water saturation and sediment properties beneath downtown SLC. When we

combine our analysis with existing data and models, we characterize the fault stepover region beneath SLC.

Setting

The Salt Lake basin is bounded by the Wasatch range to the east and Oquirrh Mountains to the west (Fig. 1). These ranges contain Precambrian bedrock, Paleozoic and Mesozoic sedimentary rocks, and Tertiary igneous and sedimentary rocks (Davis, 1983). The west-dipping WSF and Cottonwood fault appear as prominent topographic scarps separating the Salt Lake basin from the Wasatch range to the east (e.g., Bruhn *et al.*, 1992). The EBF lies between these two faults and forms a prominent intra-basin scarp. These three faults compose the 40 km long SLC segment of the WFZ. Little is known about the subsurface fault geometry of any of these faults, but geologic mapping, structural

1. Department of Geosciences, Boise State University, Boise, Idaho, U.S.A., https://orcid.org/0000-0003-2793-8173 (LML); 2. Pacific Northwest National Laboratory, Richland, Washington, U.S.A., https://orcid.org/0000-0002-3311-4114 (JSC); 3. Utah Geological Survey, Salt Lake City, Utah, U.S.A., https://orcid.org/0000-0002-9811-2283 (APM)

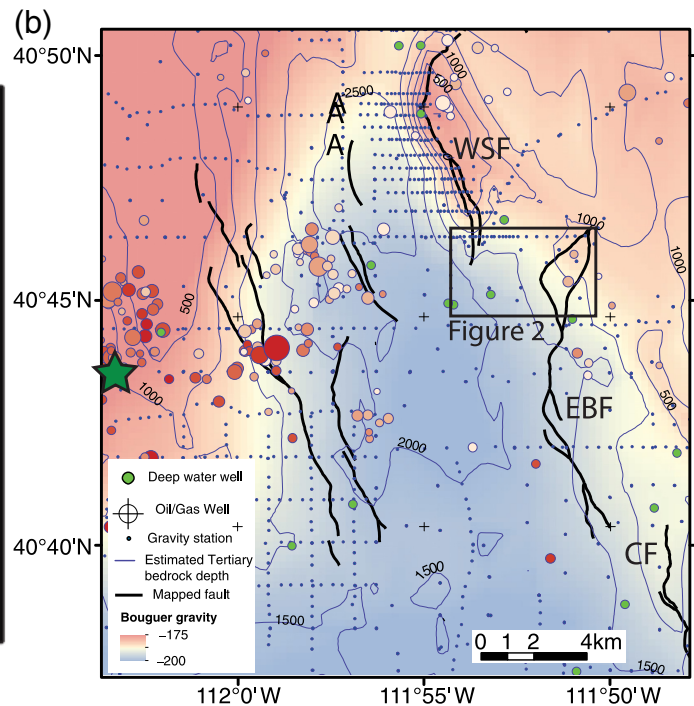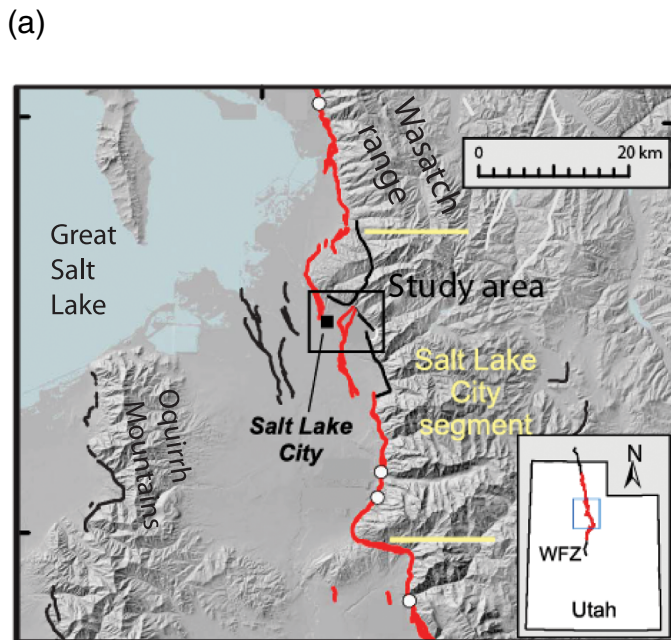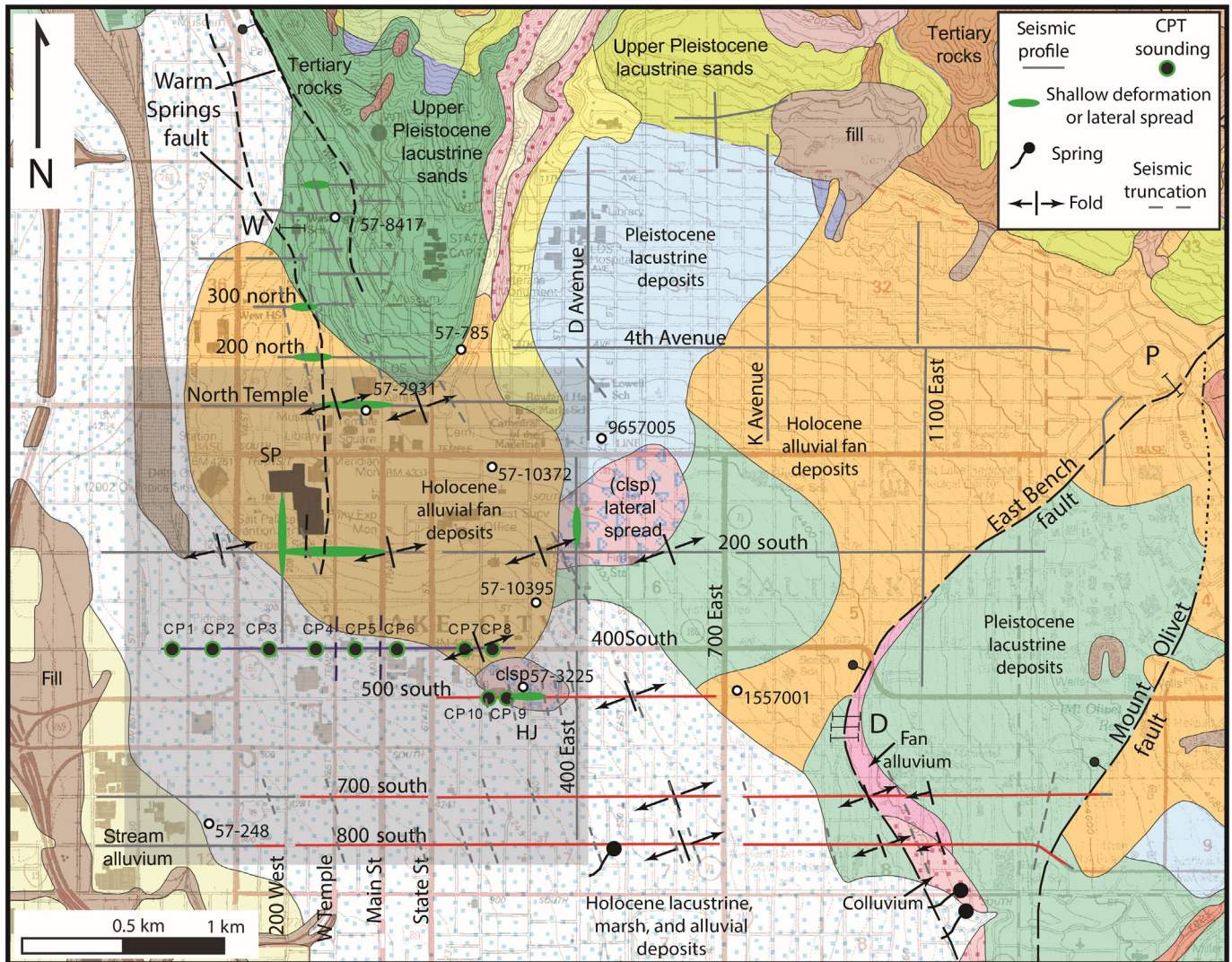*Corresponding author: lliberty@boisestate.edu

(a)

(b)

Figure 1. (a) Key active faults (red lines) along the Wasatch range front in central Utah (modified from DuRoss *et al.*, 2016). Black lines show other Quaternary active faults. Black box represents the study area. (b) Bouguer gravity map for the Salt Lake basin showing northwest-trending depth-to-bedrock contours (compiled by Roten *et al.*, 2011) that support a linkage between the East Bench fault (EBF) and Warm Springs fault (WSF). Black box represents Figure 2 region. The green star represents the 2020 Magna earthquake epicenter. Historical seismicity (red circles) shows a focus on the west side of the valley. CF, Cottonwood fault.

models, gravity data, industry seismic data, and constraints from the 2020 Magna earthquake suggest a ∼70° fault near the surface and listric fault geometry at depth (e.g., Smith and Bruhn, 1984; Bruhn *et al.*, 1992; Pang *et al.*, 2020; Kleber *et al.*, 2021). The ∼3 km left step between the active EBF and the WSF lies beneath the most densely urbanized parts of Utah, and the slip distribution and interactions between the fault strands are unclear (DuRoss *et al.*, 2016).

Lake Bonneville, the predecessor to Great Salt Lake, occupied the region from 30 to 13 ka, and consisted of transgressive, overflowing, and regressive phases (Oviatt, 2015). The deposits of Lake Bonneville are relevant to our seismic study, as they form much of the shallow stratigraphy for the Salt Lake basin consisting of alternating fine- and coarse-grained lacustrine and alluvial strata in the lower elevations, and coarse-grained, near shore deposits and alluvium near the Lake Bonneville margins (Personius and Scott, 1992; Fig. 2). Identifying deformed or vertically displaced Bonneville deposits would provide compelling evidence of active faulting and linkage between separate faults of the WFZ.

Based on circumstantial evidence, the WSF extends south of its topographic expression (DuRoss *et al.*, 2014; Fig. 2). Construction excavations at the Salt Palace Convention Center (SP, 200 south) and exploratory trenches at the Metropolitan Hall of Justice (HJ, 500 south) revealed complex faulting within latest Pleistocene post-Bonneville alluvial and Lake Bonneville

deposits (Osmond *et al.*, 1965; Simon and Shlemon, 1999). Although some have argued that the faults could have formed from liquefaction-induced lateral spreading, cone penetrometer test (CPT) soundings along 400 south provided evidence of a 3–11 m change in the elevation of Lake Bonneville sediments over about 1.2 km along 400 south, presumably related to folding or faulting (Leeflang, 2008). In addition to trench and CPT measurements, evidence to link the WSF and EBF has been hypothesized via the west–northwest-trending Virginia Street fault that lies northeast of downtown SLC (Van Horn and Crittenden, 1987) and through a normal fault relay structure (Machette *et al.*, 1992; Fossen and Rotevatn, 2016). The latter explanation would produce strain accumulation in the fault overlap zone, resulting in subparallel fractures, folds, and subsidiary faults. These relay zones can provide a conduit or barrier for fluid flow, consistent with groundwater models (e.g., Thiros, 2003) and

Figure 2. Geologic map, modified from Personius and Scott (1992), showing locations of all seismic profiles (thin gray lines). Profiles along 500 south, 700 south, and 800 south are shown as red lines. We include simplified interpretations from this study. Cone penetrometer test (CPT) soundings along 400 south and 500 south (green circled, black dot). Dashed lines represent lateral terminations identified with seismic data and align along a N20°W trend. Fold apexes (black arrows) are derived from reflection results. Green ellipses represent lateral spreading identified from anomalous Rayleigh-wave speeds. Note the lateral spread deposits along 200 south and 500 south. Downtown Salt Lake City (SLC) is the shaded gray box. The Salt Palace Convention Center (SP), Dresden Place (D), Penrose Drive (P), Metropolitan Hall of Justice (HJ), and the Washington Elementary School (W) paleoseismic trench sites and fault locations are summarized by DuRoss et al. (2014).

Interferometric Synthetic Aperture Radar (InSAR) results of Hu and Bürgmann (2020). They identify a ~N20°W-trending, low-permeability boundary that connects the WSF and EBF. These circumstantial observations and models are consistent with active faults that lie beneath downtown SLC. Here, we provide direct evidence for these faults through seismic imaging.

Seismic Data

We acquired approximately 35 km of seismic data along heavily trafficked SLC streets (Fig. 2). The data were collected at a nominal 2 m shot spacing using a 200 kg accelerated weight drop source and two-component (vertical and inline), 1.25 m spaced sensors with 4.5 Hz baseplate-coupled geophones embedded within a fire hose. The source produced broadband impulsive signals between 3 and 300 Hz. We pulled

our seismic streamer at a distance of 5 or 10 m behind the seismic source. Thus, we collected more than 15,000 48 channel shot gathers with a 60 m receiver aperture. The length of the streamer was restricted to less than the length of a city block, and this restricted length limited our imaging capabilities to late Quaternary and younger strata. Although we emphasize results along select profiles here, Liberty et al. (2018) showed results from all profiles acquired as part of this study.

We extracted vertical-component first-motion signals to obtain V_P measurements to 20–30 m depth using the approach of St. Clair (2015), two-component fundamental Rayleigh-wave dispersion curves to estimate V_S to 30 m depth using the approach of Gribler et al. (2020), and vertical-component reflection signals to map structure and stratigraphy from about 20 m depth to 300 m depth (Fig. S1). Reflection processing for land streamer data include a mix of land and marine processing approaches. Depths from travel-time images were estimated using a smoothed stacking velocity and refraction model. We utilized a differential Global Navigation Satellite System to obtain decimeter-scale position measurements during data collection. We then used 0.5 m light detection and ranging-derived (lidar) elevations for subsequent data processing. Additional details regarding our seismic approach are summarized in the supplemental material.

500 South

The 1.3 km long west to east 500 south profile typifies our seismic observations. Personius and Scott (1992) mapped late Pleistocene Lake Bonneville and younger Holocene deposits along the profile, with lateral spread deposits identified between about 200 east and 400 east (Fig. 2). Osmond et al. (1965) identified liquefaction, lateral spread deposits, and west-trending and north-trending high-angle faults, with up to 2.5 m of post-Bonneville sediment displacement from excavations at the HJ building site. However, they provided no direct evidence that the deformation was rooted in active faults, instead relating soft-sediment deformation possibly to liquefaction-induced lateral spreading.
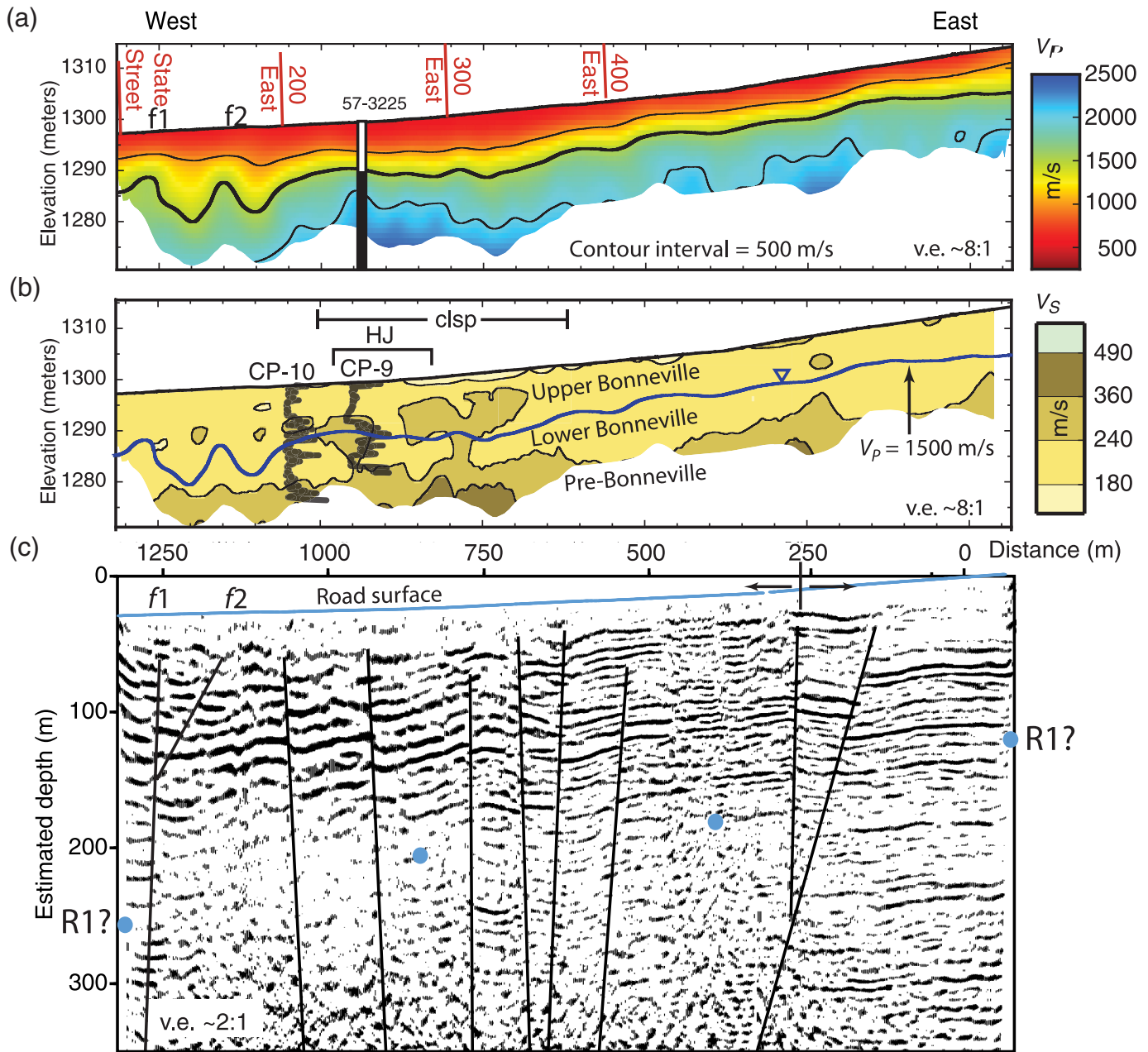
V_P ranges from about 600 m/s at the surface, gradually increasing with depth (Fig. 3). The 1500 m/s contour, our water table proxy, ranges from 8 to 15 m depth and is consistent with static water well levels. This contour parallels the ground surface along much of the profile, but it deepens and undulates along the western portion of the profile (locations $f1$ and $f2$). V_S measures mostly less than 240 m/s in the upper 10 m, except for between position 700 and 1000 m, where we map >240 m/s soil at a few

meters depth. We note a V_S decrease with depth between positions 700 and 900 m, consistent with sediment repacking from lateral spreading (Personius and Scott, 1992; Obermeier, 1996). Near the western portion of the profile, Leeflang (2008) interpreted two CPT soundings (CP-9 and CP-10) that show large lateral changes in physical properties over a distance of about 100 m. Leeflang (2008) concluded that latest Pleistocene sediments of relatively different ages and origins have been juxtaposed between the two adjacent CPT soundings. The shallow high over low-tip resistance measurements of CP-9 directly relates to faster (more stiff) V_S values overlying slower (less stiff) V_S soils. The combined CPT, V_S, and excavation observations suggest that earthquake-induced deformation followed late-stage Lake Bonneville deposition. Combining regionally low V_S values with shallow water observations, liquefaction potential remains high during future earthquakes.

The 500 south reflection image shows west-dipping and vertically offset reflectors from the near surface to about 300 m depth (Fig. 3). The Wasatch Front Community Velocity Model of Roten et al. (2011) places the Tertiary rock surface (R1) at about 130–230 m below the surface, suggesting our reflection data have captured late Quaternary structure and stratigraphy. Centered near 250 m distance, we identify the crest of a ~250 m wide fold, that lies slightly east of a similarly wide fold noted with a CPT transect located about 200 m to the north (Leeflang, 2008), and west of a similar fold identified on 700 south and 800 south seismic profiles (described subsequently). This fold is bounded by faults that offset and tilt late Quaternary strata. Although it is difficult to track reflectors across some faults, we generally observe increasing displacement with depth across both east- and west-dipping high angle faults. For example, the down-to-the-east fault below the HJ excavation site (position 950 m) shows 5–10 m reflector offsets at 100–150 m depth that is consistent with an active growth fault. We conclude that ground displacements observed at the HJ site are likely related to motion along the underlying 60°–85° east-dipping faults that offset upper Lake Bonneville and older deposits. Reflector offsets across this profile support a broad deformation zone that lies between the WSF and EBF. The high V_S zone beneath HJ is consistent with a 300 m wide zone of reworked sediments related to earthquake-induced liquefaction.
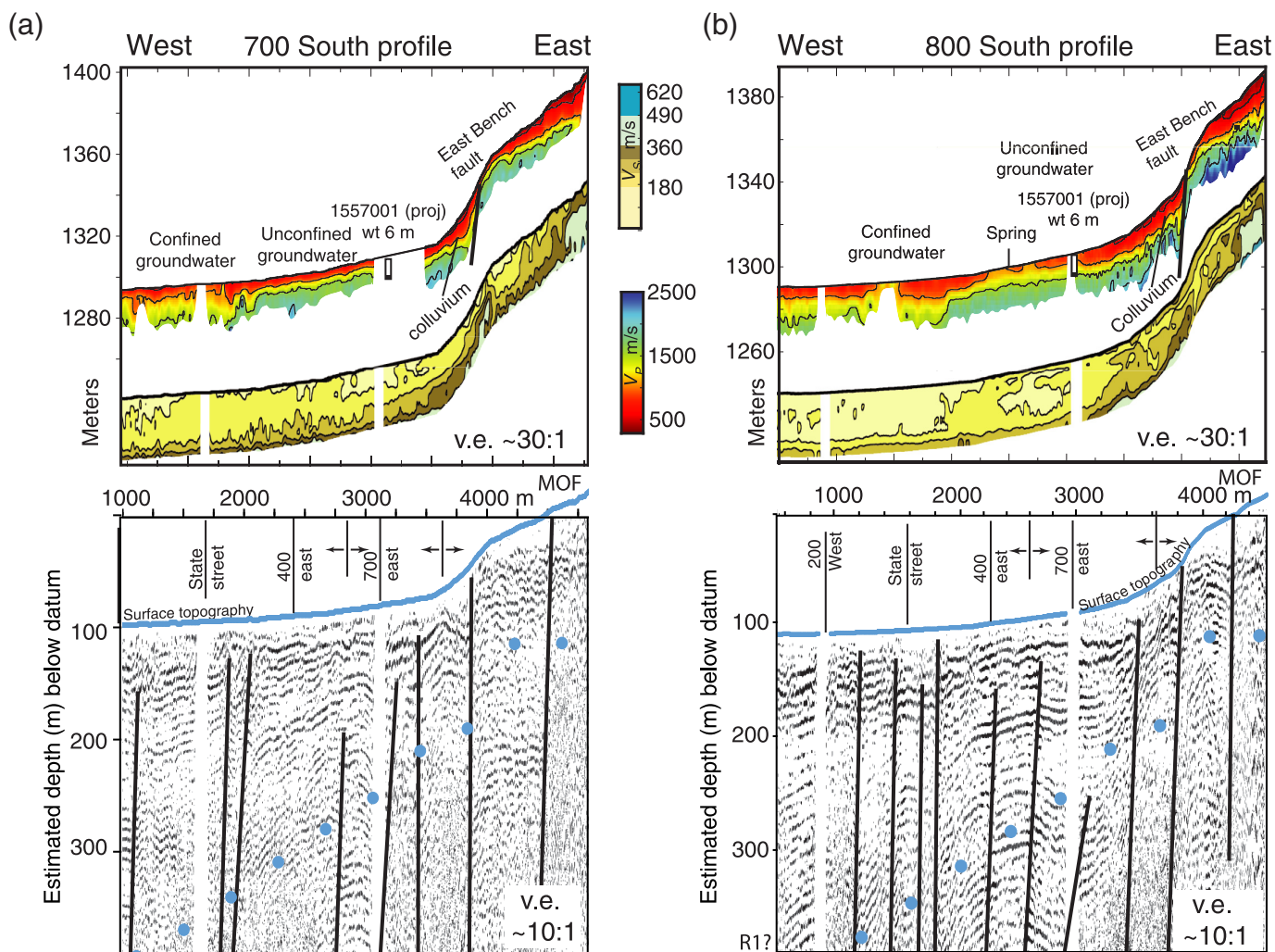
700 South/800 South

The 5 km long 700 south and 4.5 km long 800 south profiles cross the southern projection of the WSF through downtown SLC between 200 West and State Street, and crosses the EBF

(a)

West   East

Contour interval = 500 m/s   v.e. ~8:1

(b)

clsp
HJ
CP-10 CP-9
Upper Bonneville
Lower Bonneville
V_P = 1500 m/s
Pre-Bonneville
v.e. ~8:1

(c)

f1   f2   Road surface

R1?

R1?

v.e. ~2:1

Figure 3. 500 south seismic results (a) V_P first-arrival tomogram. Well 57-3225 shows late Quaternary lacustrine deposits to a completion depth of 177 m. Note the irregular 1500 m/s (bold) contour (water table proxy) at faults $f1$ and $f2$ matches the location of $f1$ and $f2$ identified on (c). (b) V_S profile from Rayleigh-wave inversions. Leeflang (2008) tip resistance curves showing less resistance with depth within the lateral spread deposits (colluvial lateral spread deposits [clsp]) region. Depth estimates for Bonneville deposits from Leeflang (2008). Bold line represents 1500 m/s V_P contour. (c) Migrated, depth converted reflection results with interpreted faults and fold. Note the offset strata across a fault mapped below the HJ trench site. Estimated depth to Tertiary strata (R1 blue dots) is from Roten et al. (2011).

near position 3800 m (Fig. 2). Although there is no topographic or geologic evidence for faulting or liquefaction linked to the WSF along either profile, there is a prominent topographic scarp related to the EBF (Fig. 4). Along each profile, Personius and Scott (1992) mapped an eastward progression of Holocene to latest Pleistocene lacustrine, marsh, and alluvial deposits (Fig. 2). West of position 3500 m on both the profiles, the surface topography slopes about 1.5°–2° to the west. Near the EBF, the surface slope increases to about 10°, then tapers off farther east. Personius and Scott (1992) mapped a 200 m

Figure 4. V_P, V_S, and reflection profiles for (a) 700 south and (b) 800 south. Note the increase in slope associated with the EBF where we identify low-V_P wedge of colluvium in the upper 10 m. Low V_P and high V_S within the EBF suggest that dry, stiff soils occupy the fault zone. Migrated, depth converted reflection results show evidence for folded and faulted late Quaternary strata to within 20 m of the surface, consistent with deformed Lake Bonneville strata. The relationship between identified faults and folds for all profiles is highlighted on Figure 5. Estimated depth to Tertiary strata (R1 blue dots) is from Roten et al. (2011). MOF, Mount Olivet fault.

wide zone of colluvium and alluvial fan deposits near the EBF. Roten *et al.* (2011) placed the top of the Tertiary strata from 100 to 300 m below the surface along these profiles (Fig. 4).

To the west of position 1500 m along 700 south and west of position 2000 m along 800 south, we measure $V_S < 180$ m/s in the upper 20 m (Fig. 4), consistent with Holocene lacustrine and marsh deposits (Personius and Scott, 1992). Here, borehole V_S measurements are consistent with our surface measurements (McDonald and Ashland, 2008; Gribler *et al.*, 2020). Above about 1295 m elevation, east of position 2000 m on both profiles, we observe an increase in V_P and V_S. We relate the abrupt lateral change in V_P to a shallower water table or a transition from confined to unconfined groundwater systems. Thiros (2003) noted this as a transition from a recharge to a discharge groundwater system, and InSAR data are consistent with a ~N20°W low-permeability, fault-derived groundwater barrier (Hu and Bürgmann, 2020).

Above an elevation of about 1310 m, or east of position 3500 m and a few hundred meters west of the EBF, we observe slower V_P and faster V_S in the upper 10–20 m depth (Fig. 4). We attribute the slower V_P to an increase in depth to water-saturated sediments and to the presence of colluvium at the base of the EBF. The faster V_S or stiffer soils are consistent with older late Pleistocene lake strata at higher basin elevations

(Personius and Scott, 1992). Immediately to the west of the EBF, we observe slower V_P and V_S, consistent with the presence of alluvium, colluvium, and lacustrine deposits. Low V_P and high V_S within the narrow faulted region suggests that dry stiff soil occupies the fault zone. In the footwall of the EBF at position 4000 m, we observe $V_P > 1500$ m/s at about 3 m depth. This V_P increase is consistent with groundwater springs (Fig. 2), and that strata in the footwall part of the EBF provide a barrier to lateral groundwater flow. Between position 4500 and 4600 m, a sharp V_S increase, coupled with a change in surface slope, is consistent with the Mount Olivet fault (McKean, 2020). We identify no V_S inversion along either profile that would support the presence of lateral spread deposits.

We map faults from our reflection profile that extend to 20 m depth, or shallower, along the length of each profile (Fig. 4). We observe kilometer-wavelength folded strata in the upper 300 m depth, consistent with late Quaternary syn- or post-deposition deformation (Fig. 4). The crest of one anticline is located between position 2500 and 3000 m, where an artesian spring is present (Fig. 2). We link this anticline to the one observed along the 500 south seismic profile and the 400 south CPT transect to identify a N20°W structural trend (also constrained from 200 south to 400 east seismic profiles; Liberty et al., 2018). Reflectors close to the EBF appear folded and have a 40 m offset along the shallowest reflector (about 20 m depth) over a distance of about 400 m. The presence of tilted strata within the EBF zone is consistent with the monoclinal warping documented in the nearby Dresden Place trenches (Machette et al., 1992; D on Fig. 2). A synclinal inflection in reflectors at position 4500 m (best seen on 800 south) is consistent with either a second strand of the EBF or related to the subparallel Mount Olivet fault (McKean, 2020). We note that fault locations and characteristics differ between the 700 south and 800 south profiles, consistent with soft sediment, noncataclastic deformation (e.g., Fossen and Rotevatn, 2016). These faults may localize and merge at depth.

Offset reflectors to within 20 m of the surface along both 700 south and 800 south profiles are consistent with a distributed zone of folding and faulting to the west of the EBF (Fig. 4). Reflector discontinuities and changing reflector dips are clear and consistent with late Pleistocene faulting beneath SLC. This observation is consistent with post-Bonneville faulting that extends to at least 1 km to the south of the current WSF mapped limit (Fig. 2; DuRoss et al., 2014). Unlike our 500 south V_S result, we find no seismic evidence consistent with lateral spreading along either profile. This observation may support

a tapering of slip along the southern limits of the WSF and transfer to the EBF beneath this part of downtown SLC.

Discussion

When we combine our interpretations with past observations, we show that the WSF and EBF are linked. The best evidence for active faulting within this left-step region is at the HJ trench site. Here, both west- and north-trending faults offset the youngest Lake Bonneville strata, and these shallow faults lie above a steep, east-dipping growth fault. This presumed antithetic fault, coupled with the other synthetic and antithetic subsidiary faults, defines a diffuse deformation zone where fault dips and displacements change across distances of a few hundred meters.

Our interpretation of linked, subparallel faults that are capable of a throughgoing rupture is not unique. Wesnousky (2008) showed many examples in which an earthquake has triggered a rupture on an adjacent fault within a fault system of similar dimensions. Many of these examples show tectonic displacements within the stepover region. One difference here is that there is no topographic fault expression within downtown SLC, suggesting that either the identified faults have not produced measurable displacements during the past few earthquake cycles (DuRoss et al., 2016) or that the topography was reset during early settlement. Given the diffuse nature of faulting, we may expect only small tectonic displacements for any one fault during a large earthquake.

The prominent fold and related faults that we identify on all three seismic profiles lies within the hanging wall of the EBF and is consistent with a rollover anticline. These structures are common with listric normal faults with active deposition (Xiao and Suppe, 1992; Pang et al., 2020). To explain the broad zone of distributed faulting, we support the relay structural model of Fossen and Rotevatn (2016). They noted that when two subparallel fault segments interact, a complex deformation zone of subsidiary faults and folds can form a topographic relay ramp, tapering slip on each fault as they overlap (Fig. 5). High-Coulomb shear stress in the relay zone would favor fault linkage near the center of the overlapping fault system or beneath downtown SLC. The presence of north- and northwest-trending subsidiary faults observed with seismic and trench data are consistent with this structural model. Surface topographic data and depth estimates to the base of Tertiary strata (Roten et al., 2011) are consistent with a southwest-dipping unbreached ramp between the WSF and EBF (Fig. 5). The Virginia Street fault (Van Horn and Crittenden, 1987) may represent a breach of this ramp.
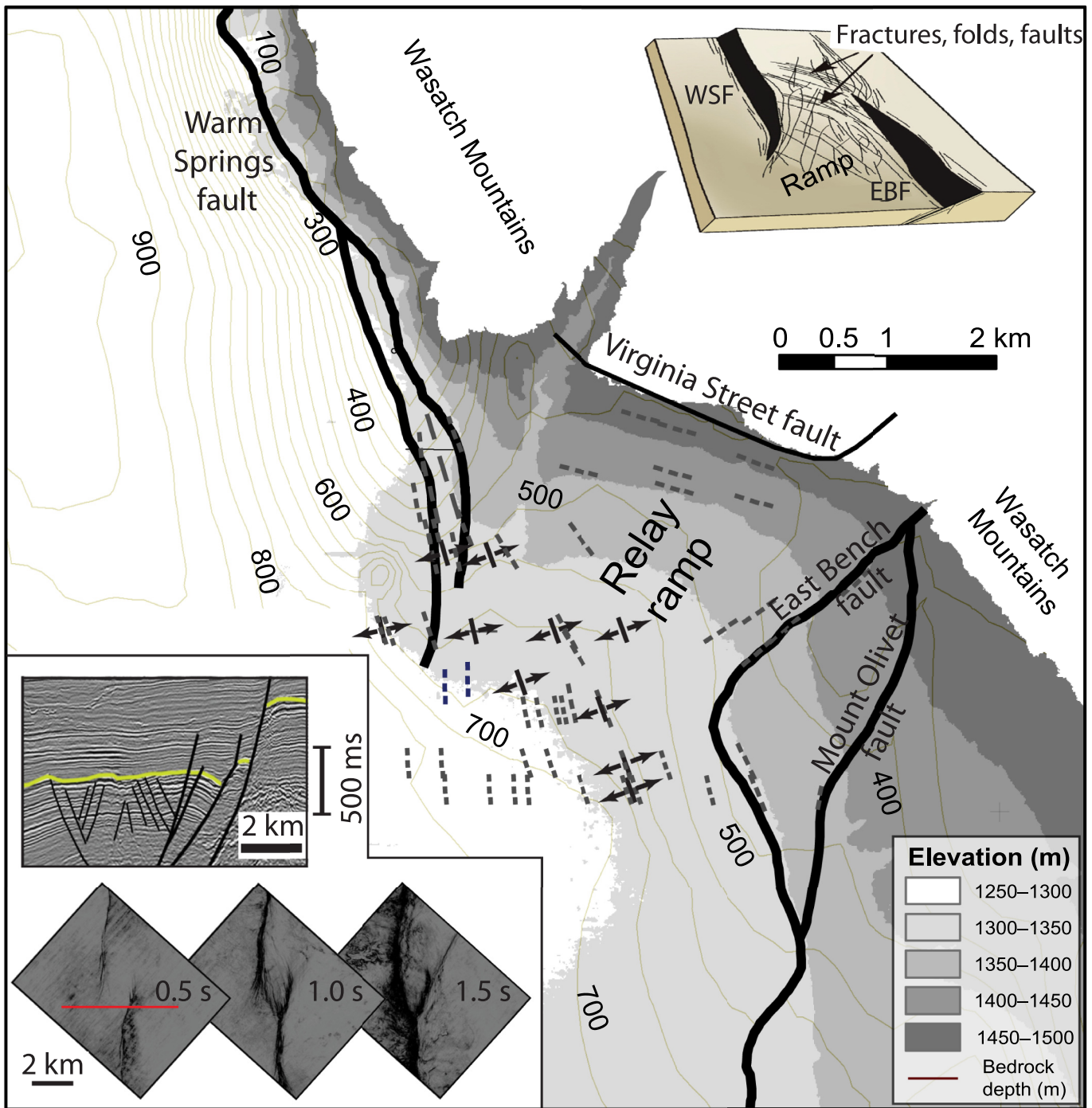
Figure 5. Mapped faults and folds from our seismic profiles and from previous studies. Select surface topography and depth to base of tertiary strata contours (Roten *et al.*, 2011) support a southwest sloping relay ramp that separates the WSF from EBF. Conceptual model (upper right inset) shows fractures, faults, and folds within an unbreached relay ramp (modified from Fossen and Rotevatn, 2016). Lower left inset shows seismic time-slice and cross-section images from the Parihaka fault (modified from Giba *et al.*, 2012). These slices are at 500 ms (~500 m depth) intervals and show two overlapping faults that link with increasing depth. Red line represents approximate cross-section location. The yellow marker horizon is offset by faults and a fold.

We use the Parihaka fault in the Taranaki basin, New Zealand, as an analog to the EBF-WSF left step (Fig. 5). Through 3D seismic data, Giba et al. (2012) showed two offset faults, mapped about 2 km apart at shallow depths. These two faults show increasing linkage with depth, with a prominent fold between the linked faults. Soliva et al. (2006) characterized the fault-zone-width (lateral distance between faults) to fault-overlap-length ratios for a range of similar fault systems. Their empirical database for a 3 km left step between the EBF and WSF would place a fault overlap length between 3 and 10 km. Regardless of how the fault tips are measured or the fault zone details, this model is consistent with the WSF extending south to at least 800 south, and through the SLC downtown corridor.

The complex distribution of faults identified at both trench sites and with our seismic data suggest a detailed stratigraphic and structural analysis is needed to fully assess each fault's slip history. Although this analysis is beyond the scope of this article and the presented dataset, the proximity of active faults, shallow water, and low V_S (loose soils) suggest that $M < 5$ earthquakes may induce liquefaction beneath downtown SLC (Ambraseys and Menu, 1988), and larger earthquakes ($M > 6.5$) may induced surface ruptures that could impact buildings not designed to handle such deformation.

Conclusions

Seismic imaging through SLC provides a catalog of faults, soil properties, and fluid distributions within a left step of two faults associated with the WFZ. We show a strong relationship of V_S to mapped geology and of V_P to groundwater elevations. We place our seismic results in the context of paleoseismic trench investigations, geologic maps, and other geophysical data to highlight structural controls needed to assess seismic hazard for the SLC area. We identify a deformation zone and relay ramp that connects two active faults of the WFZ. These observations and models suggest that surface deformation within downtown SLC may accompany a large earthquake. In addition, we identify a broad zone of lateral spread deposits that lie above the transfer zone. The proximity of paleoliquefaction to the underlying faults suggests that $M < 5$ earthquakes may induce lateral spreading beneath downtown SLC. This fault connectivity model may also relate to other WFZ segments and could help refine the surface-rupture hazard and fault connectivity along other normal fault systems.

Data and Resources

Seismic data are available at the Incorporated Research Institutions for Seismology (IRIS) as an assembled dataset (http://ds.iris.edu/ds/nodes/dmc/forms/assembled-id/) and data products are archived at the Utah Geological Survey in the GeoData Archive (https://geodata.geology.utah.gov). The Wasatch Front Community Velocity Model (CVM) is available at https://geology.utah.gov/hazards/assistance/consultants/cvm-geophysical/. Light detection and ranging (lidar) elevation data are available at https://gis.utah.gov/data/elevation-and-terrain/2013-2014-lidar/. Earthquake epicenters are from the National Earthquake Information Center (NEIC) available at https://earthquake.usgs.gov. Water well data are available at http://www.waterrights.utah.gov/wellinfo/wellsearch.asp. We used the Pan American Center for Earth and Environmental Sciences (PACES, http://gis.utep.edu/subpages/GMData.html) database, in which gravity measurements were obtained using the 1927 North American Datum (NAD 27) and were terrain-corrected using a U.S. Geological Survey-derived (USGS) digital elevation model (DEM). All websites were last accessed in February 2021. The supplemental material for this article includes our seismic approach and discussion of model uncertainties.

Declaration of Competing Interests

The authors declare no competing interests.

Acknowledgments

References

Ambraseys, N. N., and J. M. Menu (1988). Earthquake-induced ground displacements, Earthq. Eng. Struct. Dynam. **16,** no. 7, 985–1006.

Bruhn, R. L., P. R. Gibler, W. Houghton, and W. T. Parry (1992). Structure of the Salt Lake segment, Wasatch normal fault zone: Implications for rupture propagation during normal faulting, in Assessment of Regional Earthquake Hazards and Risk along the Wasatch Front, Utah, P. L. Gori and W. W. Hays (Editors),

U.S. Geol. Surv. Profess. Pap. 1500, U.S. Geological Survey, Reston, Virginia, H1–H25.

Davis, F. D. (1983). Geologic map of the central Wasatch Front, Utah, *Utah Geol. and Mineral Surv. Map* 54, available at https://ugspub.nr .utah.gov/publications/maps/m-54a.pdf (last accessed February 2021).

DuRoss, C. B., M. D. Hylland, G. N. McDonald, A. J. Crone, S. F. Personius, R. D. Gold, and S. A. Mahan (2014). Holocene and latest Pleistocene paleoseismology of the Salt Lake City segment of the Wasatch fault zone, Utah, at the Penrose Drive trench site, in *Evaluating Surface Faulting Chronologies of Graben-Bounding Faults in Salt Lake Valley, Utah––New Paleoseismic Data from the Salt Lake City Segment of the Wasatch Fault Zone and the West Valley Fault Zone––Paleoseismology of Utah*, C. B. DuRoss and M. D. Hylland (Editors), Vol. 24, Utah Geol. Surv. Spec. Stud. 149, Utah Geological Survey, Salt Lake City, Utah, 1–39.

DuRoss, C. B., S. F. Personius, A. J. Crone, S. S. Olig, M. D. Hylland, W. R. Lund, and D. P. Schwartz (2016). Fault segmentation: New concepts from the Wasatch fault zone, Utah, USA, *J. Geophys. Res.* **121,** doi: 10.1002/2015JB012519.

Fossen, H., and A. Rotevatn (2016). Fault linkage and relay structures in extensional settings—A review, *Earth Sci. Rev.* **154,** 14–28.

Giba, M., J. J. Walsh, and A. Nicol (2012). Segmentation and growth of an obliquely reactivated normal fault, *J. Struct. Geol.* **39,** 253–267.

Gribler, G., L. M. Liberty, and T. D. Mikesell (2020). High-velocity surface layer effects on Rayleigh waves: Recommendations for improved shear-wave velocity modeling, *Bull. Seismol. Soc. Am.* **110,** 279–287, doi: 10.1785/0120190120.

Hu, X., and R. Bürgmann (2020). Aquifer deformation and active faulting in Salt Lake Valley, Utah, USA, *Earth Planet. Sci. Lett.* **547,** 116,471.

Kleber, E. J., A. P. McKean, A. I. Hiscock, M. D. Hylland, C. L. Hardwick, G. N. McDonald, Z. W. Anderson, S. D. Bowman, G. C. Willis, and B. A. Erickson (2021). Geologic setting, ground effects, and proposed structural model for the March 18, 2020, Mw 5.7 Magna, Utah, earthquake, *Seismol. Res. Lett.* doi: 10.1785/0220200331.

Leeflang, B. A. (2008). Ground displacement investigations in downtown Salt Lake City, Utah, using the cone penetrometer, *M.S. Thesis*, University of Utah, Salt Lake City, Utah, 160 pp.

Liberty, L. M., J. St. Clair, and G. Gribler (2018). Seismic profiling in downtown Salt Lake City: Mapping the Wasatch fault with seismic velocity and reflection methods from a land streamer, *U.S. Geol. Surv. Final Tech. Rept.*, 21 pp., available at https://earthquake.usgs .gov/cfusion/external_grants/reports/G17AP00052.pdf (last accessed February 2021).

Machette, M. N., S. F. Personius, and A. R. Nelson (1992). Paleoseismology of the Wasatch fault zone: A summary of recent investigations, interpretations, and conclusions, in *Assessment of Regional Earthquake Hazards and Risk along the Wasatch Front, Utah*, P. L. Gori and W. W. Hays (Editors), U.S. Geol. Surv. Profess. Pap. 1500, U.S. Government Printing Office, Washington, D.C., A1–A71.

McDonald, G. N., and F. X. Ashland (2008). Earthquake site conditions in the Wasatch Front urban corridor, Utah, *Utah Geol. Surv. Spec. Study* 125, 47 pp., available at http://ugspub.nr.utah.gov/ publications/special_studies/ss-125.pdf (last accessed February 2021).

McKean, A. P. (2020). Geologic map of the Sugar House quadrangle, Salt Lake County, Utah, *Utah Geol. Surv. Map 285DM*, 27 pp., 2 plates, scale 1:24,000, doi: 10.34191/M-285DM.

Moschetti, M. P., S. Hartzell, L. Ramirez-Guzman, A. D. Frankel, S. J. Angster, and W. J. Stephenson (2017). 3D ground-motion simulations of Mw 7 earthquakes on the Salt Lake City segment of the Wasatch fault zone: Variability of long-period (T ≥ 1 s) ground motions and sensitivity to kinematic rupture parameters, *Bull. Seismol. Soc. Am.* **107,** no. 4, 1704–1723, doi: 10.1785/0120160307.

Obermeier, S. F. (1996). Use of liquefaction-induced features for paleoseismic analysis – An overview of how seismic liquefaction features can be distinguished from other features and how their regional distribution and properties of source sediment can be used to infer the location and strength of Holocene paleo-earthquakes, *Eng. Geol.* **44,** nos. 1/4, 1–76, doi: 10.1016/S0013-7952(96)00040-3.

Osmond, J. C., W. P. Hewitt, and R. Van Horn (1965). Engineering implications and geology, hall of justice excavation, Salt Lake City, Utah, *Utah Geol. and Mineral Surv. Spec. Studies No. 11*, 36 pp.

Oviatt, C. G. (2015). Chronology of Lake Bonneville, 30,000 to 10,000 yr B.P., *Quaternary Sci. Rev.* **110,** 166–171.

Pang, G., K. D. Koper, M. Mesimeri, K. L. Pankow, B. Baker, J. Farrell, J. Holt, J. M. Hale, P. Roberson, R. Burlacu, *et al.* (2020). Seismic analysis of the 2020 Magna, Utah, earthquake sequence: Evidence for a listric Wasatch fault, *Geophys. Res. Lett.* **47,** no. 18, e2020GL089798, doi: 10.1029/2020GL089798.

Personius, S. F., and W. E. Scott (1992). Surficial geologic map of the Salt Lake City segment and parts of adjacent segments of the Wasatch fault zone, Davis, Salt Lake, and Utah Counties, Utah, *U.S. Geol. Surv. Misc. Invest. Series Map I-2106*, scale 1:50,000.

Roten, D., K. B. Olsen, J. C. Pechmann, V. M. Cruz-Atienza, and H. Magistrale (2011). 3D simulations of M 7 earthquakes on the Wasatch fault, Utah, Part I: Long-period (0–1 Hz) ground motion, *Bull. Seismol. Soc. Am.* **101,** no. 5, 2045–2063.

Simon, D. B., and R. J. Shlemon (1999). The Holocene "Downtown fault" in Salt Lake City, Utah (abstract), *Abstr. Programs Assoc. Eng. Geol.* 85 pp.

Smith, R. B., and R. L. Bruhn (1984). Intraplate extensional tectonics of the eastern Basin-Range: Inferences on structural style from seismic reflection data, regional tectonics, and thermal-mechanical models of brittle-ductile deformation, *J. Geophys. Res.* **89,** 5733–5762.

Soliva, R., A. Benedicto, and L. Maerten (2006). Spacing and linkage of confined normal faults: Importance of mechanical thickness, *J. Geophys. Res.* **111,** no. B01402, doi: 10.1029/2004JB003507.

St Clair, J. (2015). Geophysical investigations of underplating at the Middle American Trench, weathering in the critical zone, and snow water equivalent in seasonal snow, *Ph.D. Dissertation*, University of Wyoming, Wyoming.

Thiros, S. A. (2003). Hydrogeology of shallow basin-fill deposits in areas of Salt Lake Valley. Salt Lake County, Utah, *U.S. Geol. Surv. Water-Res. Investig. Rept. 2003-4029* 24, available at https://pubs.er.usgs.gov/publication/wri034029 (last accessed February 2021).

Van Horn, R., and M. D. Crittenden Jr. (1987). Map showing surficial units and bedrock geology of the Fort Douglas quadrangle and parts of the Mountain Dell and Salt Lake City North quadrangles, Davis, Salt Lake, and Morgan Counties, Utah, *U.S. Geol. Surv. Misc. Invest. Series Map I-1762*, scale 1:24,000.

Wesnousky, S. G. (2008). Displacement and geometrical characteristics of earthquake surface ruptures: Issues and implications for seismic-hazard analysis and the process of earthquake rupture, *Bull. Seismol. Soc. Am.* **98,** no. 4, 1609–1632.

Xiao, H., and J. Suppe (1992). Origin of rollover, *Am. Assoc. Petrol. Geol. Bull.* **76,** no. 4, 509–529.